

NUMERICAL PERFORMANCE EVALUATION OF FAN-SUPPLIED TUBE-FIN EVAPORATORS UNDER FROSTING CONDITIONS

Diogo L. da SILVA, diogo@polo.ufsc.br

Cláudio MELO, melo@polo.ufsc.br

Department of Mechanical Engineering, Federal University of Santa Catarina
88040970, Florianópolis-SC, Brazil, +55 48 3721 9397

Christian J. L. HERMES, chermes@ufpr.br

Department of Mechanical Engineering, Federal University of Paraná
PO Box 19011, 81531990, Curitiba-PR, Brazil, +55 41 3361 3239

Abstract. Compact tube-fin evaporators are widespread used in light commercial refrigeration applications. Such systems are generally space constrained, which means that the heat exchangers must have a large area-to-volume ratio. Moreover, such applications require a below zero evaporating temperature and therefore frost often accumulates on the finned surface. The frost accumulation decreases the cooling capacity because the frost layer adds an extra thermal resistance to the heat transfer process and also an extra pressure drop to the air circuit. Understanding how frost accumulates on compact heat exchangers and how the fan-supplied air flow rate is affected by this phenomenon is a mandatory requirement not only to design robust refrigeration systems but also to devise efficient defrosting strategies. Mass, energy and momentum balances were used to reduce operational and geometric parameters. Furthermore, a quasi-steady theoretical model was developed to predict the thermo-hydraulic performance of the evaporators. The numerical results were compared with the experimental accumulated mass of frost, air pressure drop, air flow rate and cooling capacity, with all the predictions falling within the experimental band of uncertainties. In addition, the effects of progressive frost clogging and low conductivity frost layer on the overall thermal resistance was evaluated, when it was found that the former is the main cause of the cooling capacity reduction under frosting conditions.

Keywords: frosted tube-fin evaporators, thermo-hydraulic performance, mathematical model, experimental results

1. INTRODUCTION

The frost formation process relies on mass and heat transfer mechanisms which depend on operational and geometrical variables. Over the past years the prediction of the frost layer growth has become an important issue for refrigeration and air conditions applications in order to reduce their energy consumption. As showed by earlier experimental studies, Stoecker (1957) and more recently Da Silva *et al.* (2010), when frost accumulates on forced air evaporators, its thermo-hydraulic performance is depleted because of the combined increase of the thermal resistance and the air pressure drop. As a consequence, the entire refrigeration system is negatively affected, which demands periodic defrost processes to recover the original performance.

Many investigators have attempted to explain the frost formation phenomenon on evaporators. Kondepudi & O'Neil (1987) proposed one of the first numerical procedures to simulate the frost grow on domestic finned heat exchangers, however no experimental results were used to validate the model. Furthermore, Tso *et al.* (2006) developed a distributed mathematical model considering the variation of the frost layer and the temperature along the finned surface. The model was validated and showed the same trends of the experimental results. In general, frost formation models assume the phenomenon as a quasi-static process, adopt the Lewis analogy and are dependent on frost properties empirical correlations, in particular the frost density, which is strongly affected by the supercooling degree, defined by Hermes *et al.* (2009) as the temperature difference between the evaporator surface and the dew-point at the evaporator inlet. More recently, CFD techniques have also been used to predict the frost phenomenon as showed by Lenic *et al.* (2009) and Cui *et al.* (2011); however, this approach increases the model complexity and it is difficult to validate due to the experimental limitations.

Although most of the reviewed models show good agreement with the physical principles, few of them account for the air flow reduction that occurs in real refrigeration systems (see Tab. 1), which is, generally, the main cause of the cooling capacity reduction. Chen *et al.* (2003) and Aljuwayhel (2006) simulated the frost growth on tube-finned evaporators under variable air flow conditions. However, the first study was validated with experimental data collected under constant air flow conditions, while the second was applied for industrial evaporators. For these reasons, the aim of the present paper is to develop a model considering the integration between the fan and the evaporator, and validate the model using experimental data collected under the variable air conditions, over a typical range of light commercial operational conditions.

Table 1. Summary of previous research of frost formation on evaporators coils

Author	Year	Origin	Application	Approach	Real fan effect
Stoecker	1957	USA	tube-fin	experimental	No
Kondepudi & O'Neil	1987	USA	tube-fin	numerical (lumped)	No
Rite & Crawford	1991	USA	tube-fin	experimental	No
Ogawa <i>et al.</i>	1993	Japan	no-frost	experimental	No
Bejan <i>et al.</i>	1994	USA	no-frost	theoretical	No
Carlson <i>et al.</i>	2001	USA	micro-channel	experimental	No
Jhee <i>et al.</i>	2002	South Korea	tube-fin	experimental	No
Chen <i>et al.</i>	2003	Canada	thermoelectric cooler	numerical (lumped)	Yes
Seker <i>et al.</i>	2004	Turkey	no-frost	numerical (lumped)	No
Tso <i>et al.</i>	2006	Singapore	tube-fin	numerical (distributed)	No
Xia <i>et al.</i>	2006	USA	micro-channel	experimental	No
Aljuwayhel	2006	USA	industrial evaporator	numerical (distributed)	Yes
Yang <i>et al.</i>	2006	South Korea	tube-fin	numerical (distributed)	No
Ngonda & Sheer	2007	South Africa	tube-fin	numerical (distributed)	No
Zhang & Hrnjak	2009	USA	tube-fin	experimental	No
Lenic <i>et al.</i>	2009	Croatia	tube-fin	numerical (distributed)	No
Cui <i>et al.</i>	2011	China	flat surface	numerical (distributed)	No

2. MATHEMATICAL MODEL

A transient model has been developed for this work considering the evaporator control volume equivalent to a row of tubes, as show in Figure 1. Because the frost formation is a complex phenomenon, the following assumptions were made in order to obtain a suitable solution: (i) the mass and heat transfer process were considered quasi-static and unidimensionals; (ii) the temperature and the frost layer thickness was assumed uniform on both the tubes and fins; (iii) the Chilton-Colburn analogy was adopted for the heat and mass transfer process; and (iv) the air properties were considered to be uniform at the control volume inlet and exit sections.

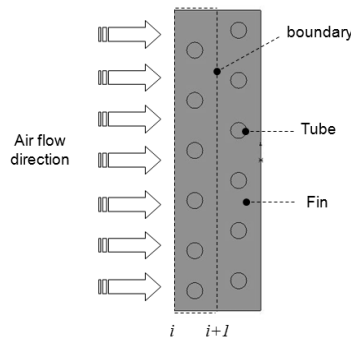


Figure 1. Schematic representation of the physical model

Therefore, mass and the energy balances over the control volume were invoked to provide one-dimension air temperature (T) and humidity ratio (ω) distributions along the coil, as follows:

$$T_{i+1} = T_{f,cv} - (T_{f,cv} - T_i) \exp\left(-\frac{\eta_f h_o A_f}{\rho_a c_{p,a} V}\right) \quad (1)$$

$$\omega_{i+1} = \omega_{sat,f,cv} - (\omega_{sat,f,cv} - \omega_i) \exp\left(-\frac{\eta_f h_o A_f}{\rho_a c_{p,a} V Le^{2/3}}\right) \quad (2)$$

where the index cv refers to the control volume (see Fig. 1), A_f is the frosted heat exchanger surface area, h_o is the air-side convective heat transfer coefficient, η_f is the frosted surface effectiveness, $c_{p,a}$ and ρ_a are the specific heat and the density of the moist air, respectively, V is the air flow rate, T_f and $\omega_{sat,f}$ are the temperature and humidity ratio (assumed to be saturated) at the frost surface, respectively, and Le is the Lewis number.

Mass and energy balances on and within the frost layer were applied to each control volume to provide the frost surface temperature (T_f) as a function of the coil surface temperature (T_s), yielding (Hermes *et al.*, 2009)

$$T_{f,cv} = T_s + \frac{Q_{sen,cv} + Q_{lat,cv}}{A_{s,cv}} \frac{x_{f,cv}}{k_f} - \frac{\rho_a \omega_{sat,s} i_{sv}}{k_f} \frac{D_{ab} \varepsilon}{\tau} \left[\cosh \left(\frac{\omega_{sat,f,cv}}{\omega_{sat,s}} \right) - 1 \right] \quad (3)$$

where k_f is the thermal conductivity of frost obtained from Lee *et al.* (1997), i_{sv} is the latent heat of desublimation, τ is the tortuosity of the frost layer obtained from the correlation of Zehnder (Na and Webb, 2004), ε is the porosity of the frost layer calculated from an empirical frost density, D_{ab} is the diffusivity of water vapor in air, and x_f is the frost layer thickness.

In addition, the sensible and latent heat transfer rates, and the air-side pressure drop at each control volume are calculated respectively from

$$Q_{sen,cv} = \rho_a c_{p,a} V (T_i - T_{i+1}) \quad (4)$$

$$Q_{lat,cv} = \rho_a i_{sv} V (\omega_i - \omega_{i+1}) \quad (5)$$

$$\Delta p_{cv} = 2C_f \rho_a \frac{L_{cv}}{D_h} \left(\frac{V}{A_{min}} \right)^2 \quad (6)$$

where C_f is the Fanning friction factor, L_{cv} is control volume length in the flow direction, A_{min} is the minimum free flow area, respectively, and D_h is the hydraulic diameter. The convective heat transfer coefficient and the friction factor were calculated from the correlations due to Wang *et al.* (2000). In order to consider the performance of a typical light commercial axial fan, the air flow rate was calculated using the fan characteristic curve (see Fig. 2), as follows:

$$V = \frac{340 - 22\Delta p + 0.57\Delta p^2 - 0.01\Delta p^3 + 4.4 \cdot 10^{-5} \Delta p^4 - 1.1 \cdot 10^{-5} \Delta p^5}{1 - 0.06\Delta p + 1.2 \cdot 10^{-3} \Delta p^2 - 1.1 \cdot 10^{-5} \Delta p^3 + 4.3 \cdot 10^{-8} \Delta p^4 - 5.5 \cdot 10^{-11} \Delta p^5} \quad (7)$$

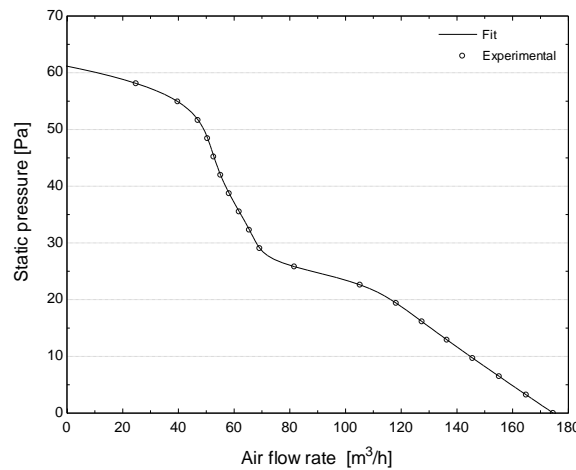


Figure 2. Characteristic curve of the fan considered in the simulations

2.2 Frost growth model

Since the frost deposition on the evaporator surface reduces the air free flow passage, as illustrated in Fig 3, the time evolution of the frost thickness should also be considered by the model. The frost growth rate is obtained dividing the overall mass flux into two terms, namely growth and densification mass fluxes, as follows (Hermes *et al.* 2009):

$$m_f = m_g + m_d = \rho_f \frac{dx_f}{dt} + x_f \frac{d\rho_f}{dt} \quad (8)$$

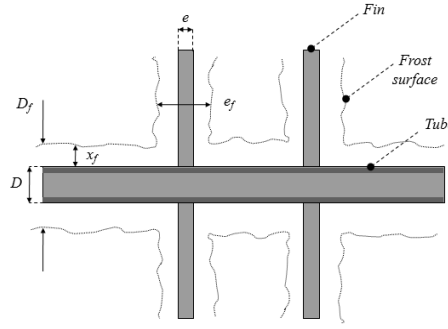


Figure 3. Schematic representation of the frosted tube-fin surface geometry

The frost density was assumed to be a function of the frost surface temperature (T_f) and the air stream dew point temperature ($T_{dew,1}$),

$$\rho_f = a \exp(bT_f + cT_{dew,1}) \quad (9)$$

Hence, it can be show that the frost thickness for each control volume is calculated at every time-step from (Hermes *et al.* 2009),

$$x_{f,cv}(t + \Delta t) = x_{f,cv}(t) + \int_t^{t+\Delta t} \frac{m_{g,cv}}{\rho_f} dt \quad (10)$$

where the mass flux of growth, m_g , is calculated as the positive real root of the following parabola (Hermes *et al.* 2009),

$$i_{sv} \frac{bx_{f,cv}}{k_f} m_{g,cv}^2 + \left(1 + \frac{bx_{f,cv}}{k_f} \frac{Q_{sen,cv}}{A_{s,cv}} \right) m_{g,cv} - \frac{Q_{lat,cv}}{A_{s,cv} i_{sv}} = 0 \quad (11)$$

2.3. Numerical scheme

An iterative procedure was used to solve the governing equations. An inner loop calculates the frost surface temperature, air pressure drop and the heat transfer rates at each control volumes, and also the air flow rate considering the fan characteristic curve (see Fig. 2), whereas an outer loop calculates the frost thickness and thus updates the evaporator geometry (see Fig. 3). Equation (10) is integrated using the adaptive predictor-corrector method introduced by Shampine and Reichelt (1997).

3. EXPERIMENTAL METHOD

2.1. Experimental apparatus

The experimental work was carried out on the test rig illustrated in Fig. 4, which consist of a rectangular cross-section closed-loop wind-tunnel and a secondary refrigeration system. The wind-tunnel controls the air temperature, humidity and flow rate at the evaporator (EVAP) inlet, while the secondary refrigeration system sets the evaporator surface temperature. The air temperature is measured by two grids of nine T-type thermocouples (TT) each, with a maximum uncertainty of $\pm 0.2^\circ\text{C}$. The relative humidity is measured by two capacitive humidity transducers (HT) that provide a maximum uncertainty of $\pm 1.5\%$. The air side pressure drop through the evaporator coil is measured by a differential pressure transducer (PT) with a maximum uncertainty of ± 2.5 Pa. The frost formation rate and the heat transfer rate are indirectly measured by mass and energy balances, with uncertainties of ± 0.1 kg/h and ± 80 W, respectively. Furthermore, the air flow rate is controlled by a variable-speed fan which emulates the behavior of the selected characteristic fan curve (see Fig.2). This strategy is used in order to account for the decrease in the air flow rate due to the reduction of the free flow area during the experiments.

The evaporator is a finned circular tube cross-flow heat exchanger, as shown in Fig. 5. The wavy-type fins are made of an aluminium alloy with a thickness of 0.2 mm with a fin density of 4 fins/cm. The copper tubes have an outer diameter of 10 mm and a wall thickness of 1 mm. The evaporator is 320 mm wide, 152 mm high and 45 mm deep. The tubes are arranged in two rows, with six tubes per row. The longitudinal and transversal spacing between two adjacent tubes are 22 mm and 25 mm, respectively.

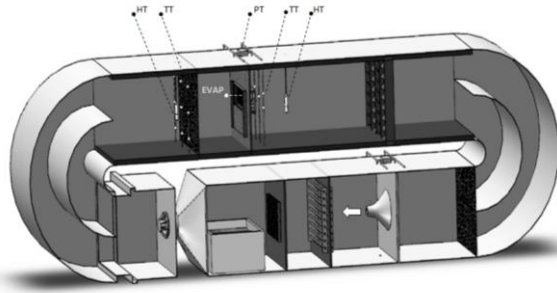


Figure 4. Schematic representation of the closed-loop wind-tunnel testing facility

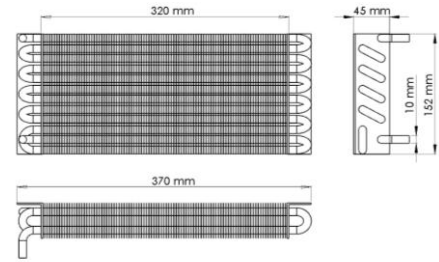


Figure 5. Schematic view of the evaporator under analysis

The tests were conducted to investigate the effect of the supercooling degree (i.e., the difference between the dewpoint and the frost surface temperature, Hermes *et al.*, 2009) on the evaporator air pressure drop, cooling capacity and accumulated frost mass. Table 1 summarizes the test conditions, which cover the ranges typical of light commercial refrigeration applications. The experimental runs were conducted until the evaporator air flow rate or the total test time reached 60 m³/h and 120 min, respectively. Further details about the experimental work description and data reduction procedure can be obtained from Da Silva *et al.* (2010).

Table 1. Summary of the experimental conditions

Test	T_1 [°C]	ϕ_1 [%]	T_s [°C]	$T_s - T_{dew,1}$ [°C]
1	7.0	85	-10.0	14.5
2	2.5	85	-10.0	10.0
3	2.5	74	-5.0	5.0

3. RESULTS AND DISCUSSION

Based on the experimental data, the coefficients $a=494 \text{ kg/m}^3$, $b=0.11^\circ\text{C}^{-1}$ and $c=-0.06^\circ\text{C}^{-1}$ of equation (9) were adjusted in order to minimize the root mean square difference between calculated and measured air-side pressure drops. Figure 6 shows a comparison between simulated and experimental accumulated frost mass. In all cases, the predictions are within a $\pm 10 \text{ g}$ error bounds indicating that the Lewis analogy provides a good estimative for the mass transfer coefficient. It can also be seen that the predicted water vapor mass flux increases with the supercooling degree, following closely the experimental trends. After 30 minutes, the accumulated frost mass for a supercooling degree of 14.5°C is two and five times higher than for supercooling levels of 10.0°C and 5.0°C, respectively. Moreover, the model is also suitable to capture the reduction of the frost growth rate over time, which is caused by the decreasing air flow rate supplied by the fan and also by the increasing frost surface temperature. Figure 7 depicts a visual comparison between the initial and final states of the exit evaporator fins referents to Test 1 conditions described in Tab. 1. The pictures show a significant reduction on the available free flow passage, which has notable influences upon the thermal-hydraulic performance of the evaporator.

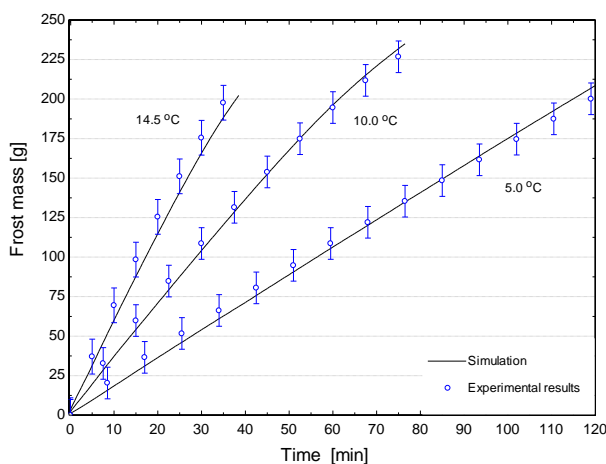


Figure 6. Comparison between simulated and experimental accumulated frost mass

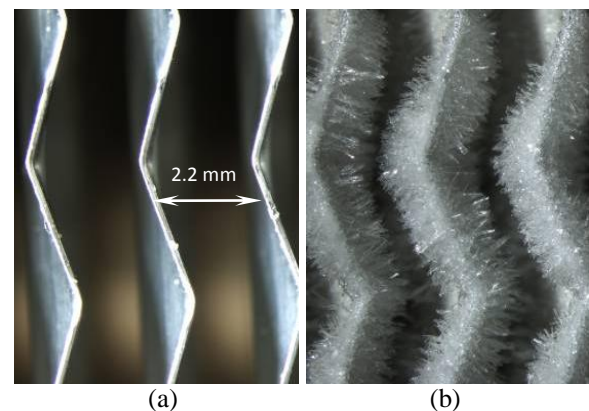


Figure 7. Visualization of the fins surface before (a) and after (b) the frost formation process in Test 1

As can be seen from Fig. 8, high supercooling degrees produce a thicker frost layer in a short period of time caused by high humidity gradients and low density frost. For instance, the case with supercooling degree of 14.5°C shows a medium frost growth rate of 1.2 mm/hour, which is considered a critical value as the initial fin space is 2.2 mm. Furthermore, in all cases the first tube column, indicated by the continuous line, developed a 35% higher frost layer in comparison with the second tube column. This difference suggests a small fin density for the first tube column to avoid a premature air flow blockage. The geometry change is also analyzed in Figure 9 using the dimensionless free flow passage ($=A_{min}/A_{face}$) evaluated at the first tube column. It can be noted that for supercooling degrees of 10.0 and 14.5°C, the evaporator is 90% and 80% blocked after 60 and 45 minutes, respectively. For a supercooling degree of 5.0°C, the evaporator becomes nearly 50% blocked in the same time period.

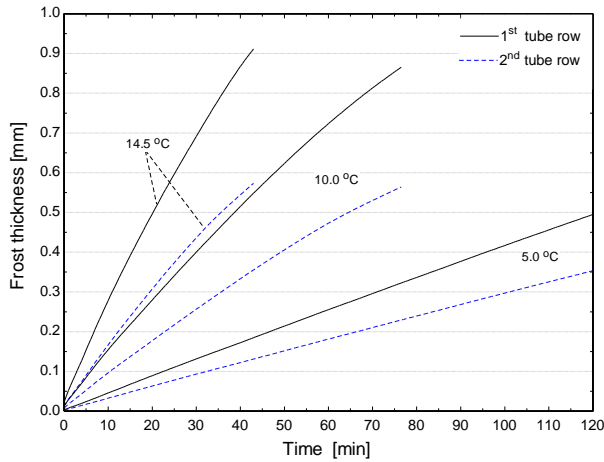


Figure 8. Calculated frost thicknesses for different supercooling degrees

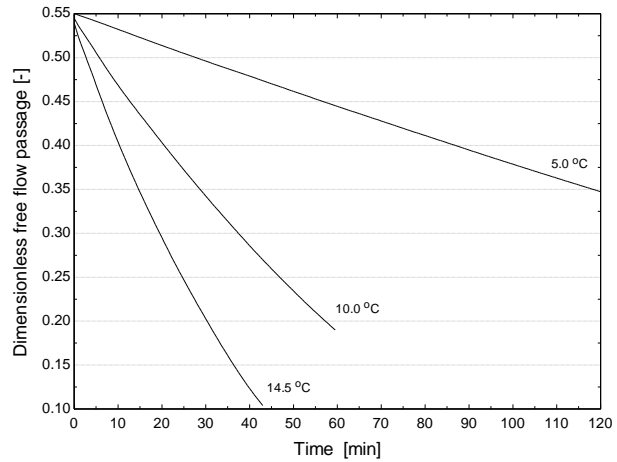


Figure 9. Calculated free flow passage for different supercooling degrees

The hydraulic performance is analysed in Figure 9, which compares the experimental and simulated results for the evaporator air pressure drop. As can be seen, the model predicts similar trends to the experimental results within a ± 2.5 Pa band of uncertainty. The inflections observed for higher supercooling degrees are associated with the fan characteristic behaviour and indicate the beginning of the stall region (see Fig. 2), where the fan efficiency starts to decrease due to the air flow detachment from the fan blades. To illustrate the influence of the pressure drop on the air flow rate, this variable is depicted in Fig. 10. In all cases, the mathematical model predictions are within the experimental uncertainty of ± 10 m³/h. Although the air flow rate has decreased only 20% with a supercooling degree of 5°C, it was observed an air flow reduction of 60% in just 40 minutes when the supercooling degree has been changed to 14.5°C. Despite the reduction in the air flow rate, Fig. 12 shows an average increase in the air flow velocity related to the evaporator minimum free flow area. This analysis shows that the rate of change in the free flow passage was greater than in the air flow rate. The only exception for this behaviour is observed after 27 and 55 minutes for supercooling degrees of 14.5°C and 10.0°C, respectively, when the air flow rate decrease is more intense due to the stall region.

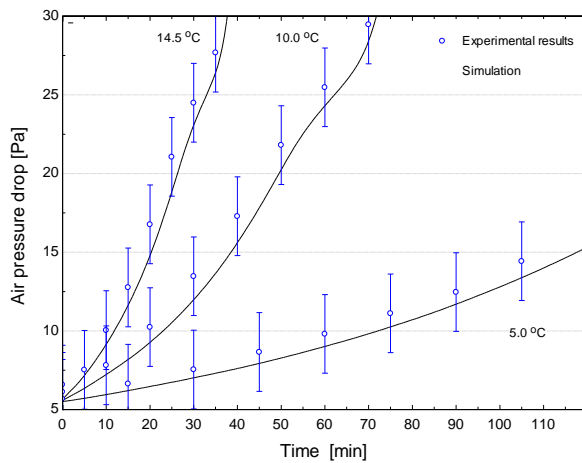


Figure 10. Comparison between simulated and experimental air-side pressure drops

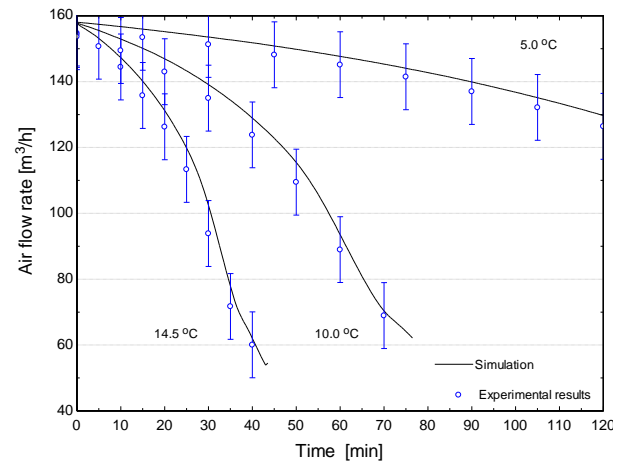


Figure 11. Comparison between simulated and experimental fan-supplied air flow rates

Turning now to the thermal performance, Fig. 13 illustrates a comparison of latent, sensible and total heat transfers between simulated and experimental results, with a supercooling degree of 10°C. In all cases, the predictions have similar pattern to the experimental data and still within a ±80 W band of uncertainty. The experimental and simulated results show a 40% total heat transfer reduction that is more intense after 50 minutes due to the beginning of the fan stall. Figure 14 presents a comparison between air side and frost layer thermal resistances. After 75 minutes, the air side thermal resistance is 6 times greater than its frost layer counterpart, pointing out the air flow reduction as the main cause of the cooling capacity depletion. In addition, the drastic increase in the air side thermal resistance, observed after 50 minutes, confirms the low fan efficiency in the stall region.

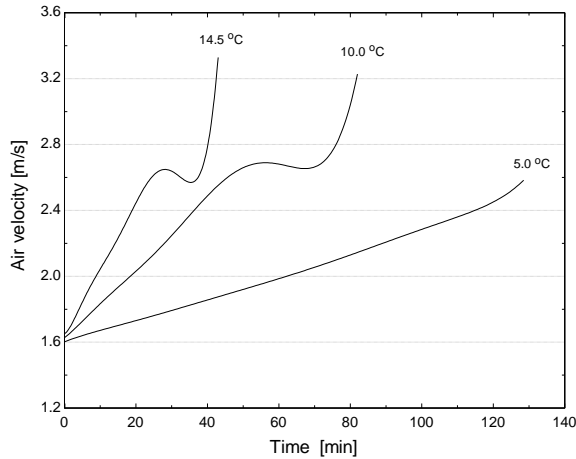


Figure 12. Simulated fan-supplied air velocities for different supercooling degrees

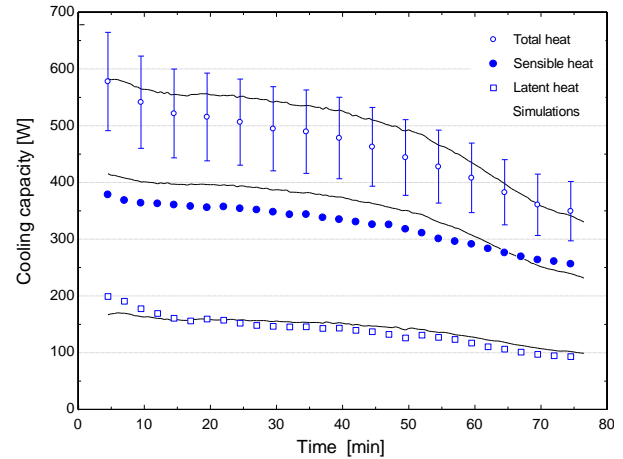


Figure 13. Comparison between simulated and experimental cooling capacities

An analysis considering the effect of frost formation on the entropy generation rate was also performed. To this end, the dimensionless entropy generation (N_S) due to heat transfer across nonzero temperature difference ($N_{S,\Delta T}$) and also to pressure drop ($N_{S,\Delta p}$) was calculated from:

$$N_S = N_{S,\Delta T} + N_{S,\Delta p} = \frac{Q_{sen} + Q_{lat}}{\rho_a c_{p,a} V} \left(\frac{1}{T_f} - \frac{1}{T} \right) + \frac{\Delta p}{\rho_a c_{p,a} T} \quad (12)$$

Figure 15 shows the dimensionless entropy generation (N_S) due to heat transfer across nonzero temperature difference ($N_{S,\Delta T}$) and also to pressure drop ($N_{S,\Delta p}$) as a function of the evaporator blockage level (i.e., $1 - A_{min}/A_{face}$). It can be seen that $N_{S,\Delta T}$ is at least an order of magnitude higher than $N_{S,\Delta p}$, showing that the frost deposition affects the heat capacity more than the pumping power. Of course, such an observation does not apply for case where a constant air flow rate is supplied by the fan. It also is worthy of note that the dimensionless entropy generation first diminishes and later increases, so that a minimum is observed. This is so as the heat transfer rate increases in the beginning of the frosting process due to an augmentation on the heat transfer surface, diminishing the thermal resistance. After a while, the frost layer gets thicker, thus both the pressure drop and the low thermal conductivity increase the thermal resistance, diminishing the heat transfer rate.

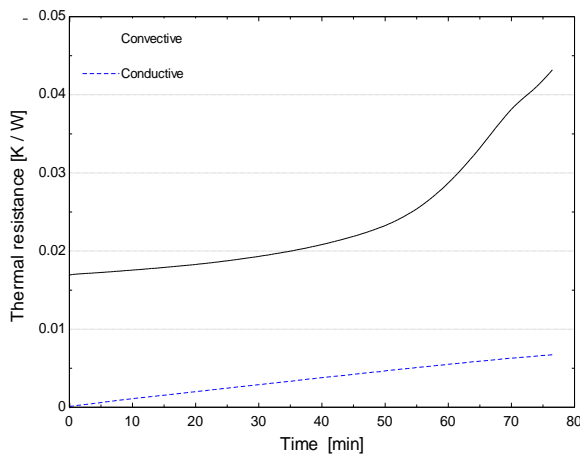


Figure 14. Comparison between convective and conductive thermal resistances

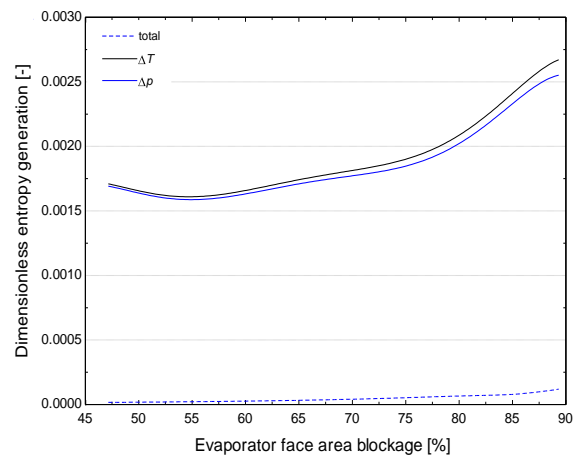


Figure 15. Variation of the dimensionless entropy generation with the face area blockage level

4. CONCLUDING REMARKS

This article has investigated the frost formation phenomenon on tube-finned evaporators taking into account the fan air flow reduction that occurs in real refrigeration systems. A mathematical model was developed to analyze the influence of operational parameters on the evaporator thermo-hydraulic performance. Experimental results, collected under variable air flow conditions, were used to validate the model showing a good agreement with the experimental uncertainties and also a suitable response to changes in the operational conditions. It was observed that high supercooling degrees increase the mass transfer rate and decrease the frost density, resulting in thicker frost layers. Furthermore, the results also suggest smaller fins density for the air entrance evaporator region. A thermal resistance evaluation showed that, under frosting conditions, the main cause for the cooling capacity decrease is the air side resistance, which increases drastically in the fan stall region. Finally, it was observed that under frosting conditions the pair fan-evaporator must be designed as a coupled system, in order to maintain the original refrigeration capacity for longer periods.

5. ACKNOWLEDGEMENTS

This study was carried out at the POLO facilities under National Grant No. 573581/2008-8 (National Institute of Science and Technology in Refrigeration and Thermophysics) funded by the CNPq Agency. Financial support from Embraco S.A. is also duly acknowledged. The authors also gratefully thank to Mr. Elias Gava Colombo and Miss Giulia Baretta, students of the Mechanical Engineering Department of the Federal University of Santa Catarina, for their valuable support in the experimental work.

6. REFERENCES

- Aljuwayhel, N. F., 2006, "Numerical and experimental study of the influence of frost formation and defrosting on the performance of industrial evaporator coils", PhD Thesis, University of Wisconsin-Madison, USA.
- Bejan, A., Vargas, J.V.C., Lim, J.S., 1994, "When to defrost a refrigerator, and when to remove the scale from the heat exchanger of a power plant", *International Journal of Heat and Mass Transfer*, Vol. 37 (3), pp. 523-532.
- Carlson, D. M., Hrnjak, P. S., Bullard, C. W., 2001, "Deposition, Distribution, and Effects of Frost on a Multi-Row Heat Exchanger Performance", Technical Report, ACRC, University of Illinois at Urbana-Champaign, USA.
- Chen, H., Thomas, L., Besant, R., W., 2003, "Fan supplied heat exchanger fin performance under frosting conditions", *International Journal of Refrigeration*, Vol. 26, pp. 140-149.
- Cui J, Li W.Z., Liu Y, Jiang Z.Y., 2011, "A new time- and space-dependent model for predicting frost formation", *Applied Thermal Engineering*, Vol. 31, pp 447-457.
- Da Silva D.L., Hermes C.J.L., Melo C., 2010, "Experimental study of frost accumulation on fan-supplied tube-fin evaporators", *Applied Thermal Engineering*, Vol. 31, pp. 1013-1020.
- Hermes, C.J.L., Piucco, R.O., Barbosa, Jr, J.R., Melo, C., 2009, "A study of frost growth and densification on flat surfaces", *Experimental Thermal and Fluid Science*, Vol. 33, pp. 371-379.
- Jhee, S., Lee, K., Kim, W., 2002, "Effect of surface treatments on the frosting/defrosting behavior of a fin-tube heat exchanger", *International Journal of Refrigeration*, Vol. 25, pp. 1047-1053.
- Kondepudi S. N., O'Neal, D. L., 1987, "The effect of frost growth on extended surface heat exchanger performance: A review", *ASHRAE Transactions*, Vol. 93, pp. 258-274.
- Lee K.S., Kim W.S., Lee T.H., 1997, "A one-dimensional model for frost formation on a cold flat surface", *International Journal of Heat and Mass Transfer*, Vol. 40, pp. 4359-4365.
- Lenic, K., Trp, A., Frankovic, B., 2009, "Prediction of an effective cooling output of the fin-and-tube heat exchanger under frosting conditions", *Applied Thermal Engineering*, Vol. 29, pp. 2534-2543.
- Na B., Webb R.L., 2004, "Mass transfer on and within a frost layer", *Int. J. Heat and Mass Transfer*, Vol. 47, pp. 899-911.
- Ngonda, T. N., Sheer, T. J., 2007, "Frost formation on cooling coil in supersaturated supply air", *International Congress of Refrigeration*, Beijing.
- Ogawa, K., Tanaka, N., Takeshita, M., 1993, "Performance improvement of plate fin-and-tube heat exchangers under frosting conditions", *ASHRAE Transactions*, Vol. 99 (1), pp 762-771.
- Rite, R.W., Crawford, R. R., 1991, "The effect of frost accumulation on the performance of domestic refrigerator-freezer finned-tube evaporator coils", *ASHRAE Transactions*, Vol. 97(2), pp. 428-437.
- Seker, D., Karatas, H., Egriçan, N., 2004, "Frost formation on fin-and-tube heat exchangers. Part I – Modeling of frost formation on fin-and-tube heat exchangers", *International Journal of Refrigeration*, Vol. 27, pp. 367-374.
- Shampine L.F., Reichelt M.W., 1997, "The Matlab ODE Suite", *Journal on Scientific Computing* Vol. 18, pp. 1-22.
- Stoecker, W.F., 1957, "How frost formation on coils affects refrigeration systems", *Refrigerating Engineering*, Vol. 65, no. 2.
- Tso, C. P., Cheng, Y. C., Lai, A. C. K., 2006, "Dynamic behavior of a direct expansion evaporator under frosting condition. Part I. Distributed model", *International Journal of Refrigeration*, Vol. 29, pp. 611-623.

- Wang C.C., Chi K.Y., Chang C.J., 2000, "Heat transfer and friction characteristics of plain fin-and-tube exchangers, Part II: Correlation", International Journal of Heat and Mass Transfer, Vol. 43, pp. 2693-2700.
- Xia, Y., Zhong Y., Hrnjak, P.S., Jacobi, A.M., 2006, "Frost, defrost, and refrost and its impact on the air-side thermal-hydraulic performance of louvered-fin, flat-tube heat exchangers", Int. J. of Refrigeration, Vol. 29, pp. 1066-1079.
- Yang, D., Lee K., Song, S., 2006, "Fin spacing optimization of a fin-tube heat exchanger under frosting conditions", International Journal of Heat and Mass Transfer, Vol. 49, pp. 2619-2625.
- Zhang, P., Hrnjak P. S., 2009, "Air-side performance evaluation of three types of heat exchangers in dry, wet and periodic frosting conditions", International Journal of Refrigeration, Vol. 32, pp. 911-921.

7. NOMENCLATURE

Roman

A_{face}	evaporator face area [m ²]
A_{min}	evaporator minimum free flow area [m ²]
A_s	evaporator surface area [m ²]
C_f	Fanning friction factor [-]
c_p	specific heat at constant pressure [J kg ⁻¹ K ⁻¹]
cv	control volume
D	external tube diameter [m]
D_{ab}	diffusivity of water vapor in air [m ² s ⁻¹]
e	fin thickness [m]
h_o	convective heat transfer coefficient [W m ⁻² K ⁻¹]
i_{sv}	frost latent heat of desublimation [kJ kg ⁻¹]
k_f	thermal conductivity of frost [W m ⁻¹ K ⁻¹]
L	control volume length [m]
Le	Lewis number ($=\alpha\epsilon\tau^{-1}D$) [-]
m	water mass flux [kg _v m ⁻² s ⁻¹]
N_s	dimensionless entropy generation rate [-]
Q	heat transfer rate [W]
T	temperature [K]
V	air flow rate [m ³ s ⁻¹]
x_f	frost thickness [m]

Greek

α	thermal diffusivity [m ² /s]
ϕ	relative humidity [%]
ϵ	frost porosity [-]
η_s	the overall surface effectiveness [-]
ρ	density [kg m ⁻³]
τ	frost tortuosity [-]
ω	humidity ratio [kg _v kg _a ⁻¹]

Subscripts

1	evaporator inlet air
d	densification
f	frost surface
g	growth
h	hydraulic diameter
i	control volume position
lat	latent
s	coil surface
sen	sensible
v	water vapor